

Mixing, upwelling, and internal wave generation beneath Super Typhoon Mangkhut: a vorticity-divergence view of the ocean response to tropical cyclones

NOEL G. BRIZUELA*, T. M. SHAUN JOHNSTON, MATTHEW H. ALFORD, OLIVIER ASSELIN, DANIEL L. RUDNICK

Scripps Institution of Oceanography, University of California, San Diego, La Jolla CA, USA

JAMES N. MOUM

College of Earth, Ocean and Atmospheric Science, Oregon State University, Corvallis, OR, USA

ELIZABETH J. THOMPSON

NOAA Physical Sciences Laboratory, Boulder CO, USA

ABSTRACT

Tropical cyclones (TCs) are powered by heat fluxes across the air-sea interface, which are in turn influenced by subsurface physical processes that can modulate the intensity of these storms and thus introduce uncertainty to weather forecasts. This study uses data from an array of 6 profiling floats to produce a three-dimensional diagnosis of ocean dynamics beneath Super Typhoon Mangkhut as it swept over the Western North Pacific in September of 2018. Vertical profiles of temperature show the mixed layer deepen ahead of the storm and reveal an asymmetric cold wake of sea surface temperature (SST). The divergence of measured horizontal currents suggests upwelling velocities of roughly 8 mh^{-1} behind Mangkhut, marking the generation of a large amplitude ($\sim 75 \text{ m}$ crest to trough) near-inertial internal wave. Furthermore, density overturns provide indirect estimates of diapycnal diffusivities $\kappa \sim 10^{-2}$ as the ocean mixed layer deepened near the TC's eye. To explain these observations, we formulate the ocean's mixed layer dynamics in terms of vorticity and divergence. This demonstrates that near-inertial oscillations transform wind-forced vorticity into divergence and thus control the timing and intensity of upwelling and internal wave generation behind fast-moving storms. Lastly, we find evidence that turbulent fronts propagated away from the storm track in phase with internal waves of frequency $\sim 2f$. Our analyses provide a rare observational confirmation of theory and comprehensive review of the subsurface physical processes controlling air-sea interactions under fast-moving TCs.

1. Introduction

Wind-powered ocean motions that oscillate near the inertial frequency f dominate upper ocean dynamics beneath and behind tropical cyclones (TCs) (Price 1981, 1983; Shay et al. 1989, 1998; Sanford et al. 2011). On the right (left) side of Northern (Southern) hemisphere storms, transient winds amplify the magnitude of these motions, but suppress them on the opposite side (Chang and Anthes 1978; Price 1981). Through turbulence and advection, these three-dimensional (3D) motions redistribute heat across subsurface reservoirs and ultimately cool the ocean surface. In turn, the heat-depleted ocean surface can inhibit sensible and latent heat fluxes across the air-sea interface, thus suppressing deep convection in the atmosphere and modulating storm intensity (Emanuel 1999; Schade and Emanuel 1999; Glenn et al. 2016).

Although most TCs leave cold wakes behind them, the sign, magnitude, and spatial distribution of sea surface temperature (SST) anomalies induced by TCs are determined by a combination of storm characteristics and preceding ocean conditions (Chang and Anthes 1978; Jaimes and

Shay 2009; Vincent et al. 2012b; Balaguru et al. 2012; Johnston et al. 2020). While the turbulent entrainment of cold and deep water into the mixed layer is often the primary contributor to upper ocean cooling (Price 1981; D'Asaro 2003; D'Asaro et al. 2007; Sanford et al. 2011; Vincent et al. 2012a), the effects of upwelling and air-sea heat fluxes can dominate under slowly-moving and low-intensity storms respectively (Vincent et al. 2012a; Yablonsky and Ginis 2009; Zedler 2009). Moreover, deeper mixed layers can reduce the subsequent sea surface cooling (Mei et al. 2015a), so the mechanisms of air-sea coupling under TCs must be assessed in a regional and storm-by-storm basis (Balaguru et al. 2012; Vincent et al. 2012b; Mei et al. 2015b).

Since the 1980s, numerous experiments have placed instruments (both intentionally and fortuitously) beneath TCs and measured the ocean's response to their extreme winds (Shay et al. (1989, 1998); D'Asaro (2003); Powell et al. (2003); D'Asaro et al. (2007); Sanford et al. (2011); Chang et al. (2013); Guan et al. (2014); Johnston et al. (2020)). Such observations have validated the results of pioneering theoretical and numerical analyses put forward by Geisler (1970); Chang and Anthes (1978) and Price (1981, 1983).

*Corresponding author: Noel G. Brizuela, nogutier@ucsd.edu

Nevertheless, our understanding of processes such as air-sea energy transfer, upwelling, mixing, and internal wave generation under TCs continues to evolve.

In this article, we use data from six profiling floats (Johnston et al. 2020) to reconstruct the 3D fields of temperature (T), salinity (S) and subsurface currents (u, v, w) beneath Super Typhoon Mangkhut (Fig. 1). Mangkhut originated on September 7 of 2018 as a tropical depression in the Central Pacific Ocean and later intensified as it moved into the Philippine Sea. Between September 11 and 15, the TC sustained maximum 1-minute wind speeds above 70 m s^{-1} , equivalent to a category 5 hurricane, while our floats sampled the ocean below (Fig. 1.b). Throughout its lifespan, Mangkhut caused substantial damages and loss of lives in the Philippines, Guam, Taiwan, Hong Kong and China (Wamsley 2018).

Under the assumption that the upper ocean response to TC forcing is steady in storm-following coordinates (Geisler 1970), we diagnose the roles of upwelling, advection, and mixing in the redistribution of heat under Mangkhut. Consistent with established theory, our analyses show the generation and subsequent propagation of a near-inertial internal wave (NIW) train in the storm's wake, as well as super-inertial waves with frequencies $> 2f$. We demonstrate that NIW generation can be diagnosed through the near-inertial coupling of upper ocean vorticity ζ and divergence Γ as the latter pumps the ocean thermocline. Lastly, we use a variety of methods to make inferences about the intensity and spatiotemporal extent of vertical mixing induced by the storm.

Section 2 discusses the mathematical theory used to understand the observed upper ocean response to TCs, while Section 3 describes our data and methodology. The spatiotemporal evolution of T and S under Mangkhut is described in Section 4, while Section 5 describes the wind-forced circulation. Patterns and mechanisms of NIW generation are demonstrated in Section 6, while Section 7 summarizes previous sections in the context of vertical mixing. Lastly, Section 8 presents a brief summary of our findings and draws conclusions on their relevance to the current state of knowledge about the ocean response to TCs.

2. Background theory

The relative contributions to upper ocean thermodynamics made by different mechanisms can be diagnosed using the advection-diffusion scheme

$$\frac{\partial T}{\partial t} = - \left(u \frac{\partial T}{\partial x} + v \frac{\partial T}{\partial y} \right) - w \frac{\partial T}{\partial z} + \frac{\partial}{\partial z} \left(\kappa \frac{\partial T}{\partial z} + Q_{atm} \right) \quad (1)$$

$$\frac{\partial S}{\partial t} = - \left(u \frac{\partial S}{\partial x} + v \frac{\partial S}{\partial y} \right) - w \frac{\partial S}{\partial z} + \frac{\partial}{\partial z} \left(\kappa \frac{\partial S}{\partial z} + J_{atm} \right). \quad (2)$$

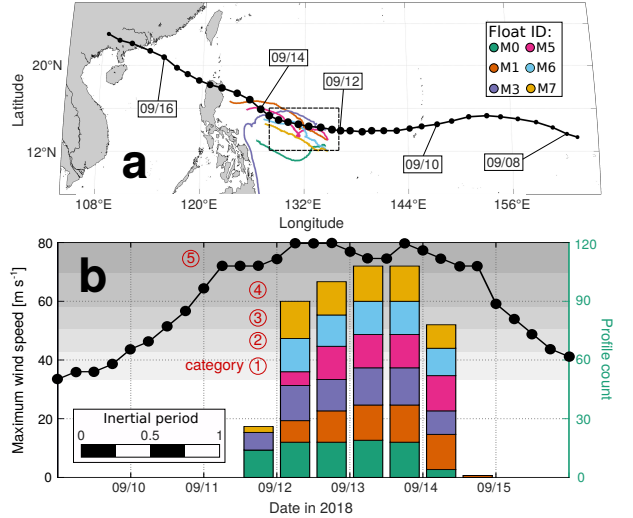


FIG. 1. Data from the Joint Typhoon Warning Center (JTWC) show the evolution of Mangkhut's track (a) and maximum 1-minute sustained wind speed $|U_{10}|$ (b, left axis and black line). The histogram in panel b (right axis) shows that float measurements used in this study (Figure 3.b) were made during Mangkhut's period of maximum intensity. Gray shading in panel b shows the wind limits for Saffir-Simpson storm Categories 1 ($|U_{10}| \leq 30 \text{ m s}^{-1}$) to 5 ($|U_{10}| > 70 \text{ m s}^{-1}$).

In this view, we track the temporal evolution of $T(x, y, z, t)$ as influenced by 3D ocean currents (u, v, w) and interactions with the atmosphere. The net surface heat flux across the air-sea interface is represented by Q_{atm} , while J_{atm} describes the salinity fluxes into the ocean that result from rainfall and evaporation. Turbulent entrainment of deep water into the upper ocean is parameterized using a vertical diffusivity κ that acts upon the gradients $\frac{\partial T}{\partial z}$ and $\frac{\partial S}{\partial z}$. Therefore, the vertical advection of isotherms $w \frac{\partial T}{\partial z}$ (upwelling) has a two-fold effect on SST; it can bring cold, subthermocline waters to the ocean surface, and also sharpen the thermal interface at the base of the mixed layer. The latter enhances the upper ocean cooling effects of shear-driven turbulence (Yablonsky and Ginis 2009; Julien et al. 2012; Vincent et al. 2012a).

a. Mixed layer models

In a simpler representation of upper ocean thermodynamics, Price (1981) defined a mixed layer of thickness $h[x(t), y]$ and used vertically-averaged forms of Equations (1) and (2) to describe the evolution of \bar{T} and \bar{S} . Here, the overbar indicates a vertical average within the mixed layer

$$\frac{\partial \bar{T}}{\partial t} = -\bar{u} \frac{\partial \bar{T}}{\partial x} - \bar{v} \frac{\partial \bar{T}}{\partial y} + \frac{Q_{am}}{h} + \frac{\delta T W_e}{h} \quad (3)$$

$$\frac{\partial \bar{S}}{\partial t} = -\bar{u} \frac{\partial \bar{S}}{\partial x} - \bar{v} \frac{\partial \bar{S}}{\partial y} + \frac{J_{am}}{h} + \frac{\delta S W_e}{h}. \quad (4)$$

The relation between time and space is given by $x = U_{storm}t$, as the TC moves along its track at speed U_{storm} . Hence, x and y define the along-track and cross-track dimensions respectively. The entrainment rate W_e represents turbulent mixing as a flux of thermocline waters with temperature $\bar{T} + \delta T$ and salinity $\bar{S} + \delta S$ into the upper ocean. This formulation implies the equivalence $\kappa \frac{\partial T}{\partial z} \Big|_{z=h} = \delta T W_e$, so that turbulent heat fluxes $\kappa \frac{\partial T}{\partial z}$ through a highly-stratified transition layer parameterize the thermal effects of cold, deep water that enters the mixed layer.

Simple layer-based models cannot accurately reproduce the effects of upwelling on SST (Yablonsky and Ginis 2009). Nevertheless, the linear response of horizontal currents $\bar{\mathbf{u}} = (\bar{u}, \bar{v})$ to a wind stress $\tau = (\tau_x, \tau_y)$ (Pollard and Millard Jr 1970) provides valuable information about vertical motions w forced by TCs (Geisler 1970).

$$\frac{\partial \bar{u}}{\partial t} = f\bar{v} + \frac{\tau_x}{\rho_0 h} - r\bar{u} \quad (5)$$

$$\frac{\partial \bar{v}}{\partial t} = -f\bar{u} + \frac{\tau_y}{\rho_0 h} - r\bar{v} \quad (6)$$

$$\frac{\partial h}{\partial t} + h \left(\frac{\partial \bar{u}}{\partial x} + \frac{\partial \bar{v}}{\partial y} \right) = W_e \quad (7)$$

More precisely, the continuity equation (7) can be used to describe vertical velocities $\frac{\partial h}{\partial t}$ of the mixed layer base as caused by divergent flows $\nabla \cdot \bar{\mathbf{u}} = \left(\frac{\partial \bar{u}}{\partial x} + \frac{\partial \bar{v}}{\partial y} \right)$ and mixing W_e . Equations (5) and (6) use the damping coefficient r to represent the loss of momentum at a given location by a combination of downward wave propagation, nonlinear effects, and turbulent dissipation (Pollard and Millard Jr 1970; D'Asaro 1985; Guan et al. 2014; Johnston et al. 2016). Furthermore, we ignore the effects of horizontal pressure gradients in the mixed layer, which can influence horizontal flows but scale to make a negligible contribution to vertical velocities (Eq. 7) given the large horizontal scale of TCs (Geisler 1970; D'Asaro 1989).

When the divergent component of the mixed layer flow oscillates slightly above the inertial frequency f , periodic displacements of the mixed layer base (Eq. 7) propagate downwards into the ocean interior as NIWs (Price 1983; Gill 1984; Shay et al. 1989, 1998). In the past, authors have represented the baroclinic ocean response to TCs by coupling contiguous layers of increasing density through the pressure gradients produced by interfacial displacements (Geisler 1970; Price 1981, 1983). However, as noted above, we represent the energy flux across the mixed layer base using a damping coefficient r that parameterizes a variety of processes that drive Eulerian momentum decay. Historically, the value of r has been thought to be determined by the rate of downward energy propagation

by NIWs, which requires the development of spatial gradients in \mathbf{u} to pump the mixed layer base (Kunze 1985; D'Asaro 1985, 1989; Alford et al. 2016). The spatial structure of TC winds imprints gradients on the upper ocean and thus allows for immediate downward energy propagation (D'Asaro 1989). In contrast, surface currents powered by mid-latitude storms often depend on planetary and mesoscale vorticity gradients to slowly develop the horizontal gradients necessary for NIWs to propagate across the ocean thermocline (Kunze 1985; D'Asaro 1989; Asselin and Young 2020).

b. Dynamics of wind-forced gradients in the upper ocean

In this section, we modify the slab layer model of Equations (5) - (7) to isolate the components that can contribute to interfacial displacements $\frac{\partial h}{\partial t}$, or pumping of the mixed layer base, in the wake of a TC. In other words, we calculate the divergence $\Gamma = \nabla \cdot \bar{\mathbf{u}} = \frac{\partial \bar{u}}{\partial x} + \frac{\partial \bar{v}}{\partial y}$ of mixed layer motions and study its relation to the vortical component $\zeta = \nabla \times \bar{\mathbf{u}} = \frac{\partial \bar{v}}{\partial x} - \frac{\partial \bar{u}}{\partial y}$. Taking the curl and divergence of Equations (5) and (6) together with (10) thus yields an alternative representation of mixed layer dynamics

$$\frac{\partial \zeta}{\partial t} = -f\Gamma + \frac{1}{\rho_0 h} \left(\nabla \times \tau + \frac{\tau}{h} \times \nabla h \right) - r\zeta \quad (8)$$

$$\frac{\partial \Gamma}{\partial t} = f\zeta + \frac{1}{\rho_0 h} \left(\nabla \cdot \tau + \frac{\tau}{h} \cdot \nabla h \right) - r\Gamma \quad (9)$$

$$\frac{\partial h}{\partial t} + h\Gamma = W_e. \quad (10)$$

This formalism does not include information about the magnitude and direction of currents. Instead, we try to resolve spatiotemporal patterns in $\frac{\partial h}{\partial t}$ and the subsequent generation of internal waves. Because Γ and ζ are only coupled by f , when we ignore terms including ∇h , Equations (8, 9) predict that the instantaneous accelerations of ζ and Γ under a TC will mirror the spatial structures of tangential and radial winds respectively (Fig. 2).

More precisely, regions of upwelling directly beneath a fast-moving storm will be mostly determined by radial winds ($\nabla \cdot \tau \neq 0$) but later influenced by both radial and tangential stresses once f couples the vortical and divergent modes of motion. If winds persist relatively unchanged over a fixed location, the upper ocean may reach an Ekman balance so that radial winds will induce a vortical circulation while tangential winds ($\nabla \times \tau \neq 0$) elicit a divergent response (Fig. 2.b). The latter process can occur under slowly-translating storms and cool SST drastically, as stationarity allows for a balance between $f\Gamma$ and $\nabla \times \bar{\tau}$ in Equation (8). Through this mechanism, cold waters are brought up through the ocean thermocline to penetrate and replace the warm water of the mixed layer (Yablonsky and Ginis 2009; Zedler 2009; Guan et al. 2014). Differences

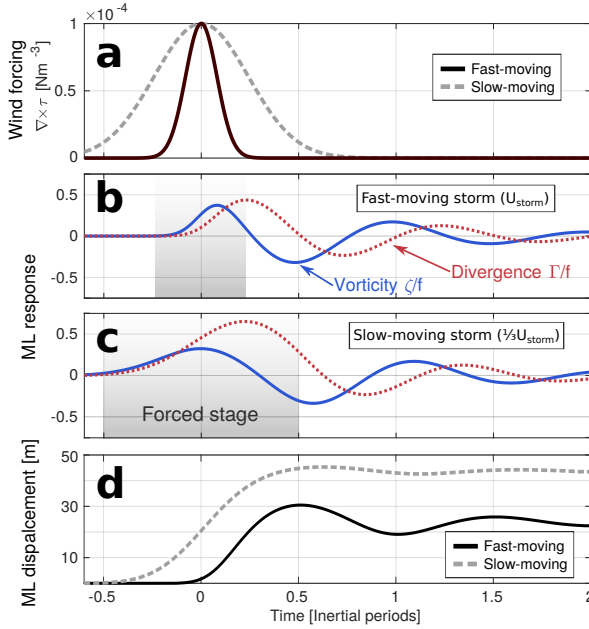


FIG. 2. Mixed layer response (Equations 8-10) to the tangential winds ($\nabla \times \vec{\tau}$, panel **a**) of a fast-moving TC (panel **b**) and one moving at one-third the speed (panel **c**) in the absence of turbulent mixing ($W_e = 0$). Panel **d** compares the mixed layer displacements $h(t) - h(t_0)$ that result from both storms, where upwelling causes positive displacements. Gray shading in panels **b,c** marks the forced stage, which is followed by near-inertial pumping of the mixed layer base.

between the mixed layer response to fast- and slow-moving TCs are shown in Figure 2.

In the wake of a storm, once winds cease to play a dominant role and mixed layer motions are left to evolve freely, our diagnostic model predicts the three-term balance

$$\frac{\partial \zeta}{\partial t} = -f\Gamma - r\zeta \quad (11)$$

$$\frac{\partial \Gamma}{\partial t} = f\zeta - r\Gamma. \quad (12)$$

This linear system of equations, a damped harmonic oscillator, produces cycles that alternate through ζ and Γ at the inertial frequency but whose amplitude decays with an e-folding time scale r^{-1} .

Consistent with the generation of NIWs, pressure gradients caused by changes in h (Fig. 2.d, Eq. 10) will impart momentum to deeper regions of the ocean. These simple dynamics also hint at the cancellation of Ertel potential vorticity, which defines internal waves in the absence of diabatic processes and background vorticity. As laid out by Pinkel (2014) and Lien and Sanford (2019), this essentially requires that variations in ζ be balanced by isopycnal stretching, which is in turn driven by Γ (Sun and Kunze 1999; Alford and Pinkel 2000).

Internal waves generated by TCs have been observed using autonomous profiling sensors and moored instruments alike (see for instance Shay et al. (1989); Sanford et al. (2011); Guan et al. (2014); Pallàs-Sanz et al. (2016) and references therein). However, observational studies rarely capture the spatial structure of NIWs, which is otherwise diagnosed using numerical models (Shay et al. 1998; Zedler 2009; Voelker et al. 2019). Because NIWs are not exactly inertial, knowledge of their wavenumber vector $\vec{k} = [k, l, m]$ is crucial to assess their frequency and propagation through the stratified ocean (Garrett 2001; Alford et al. 2016; Johnston et al. 2016). Observational estimates of NIW structure such as the ones derived in this study can inform rates of Eulerian momentum decay driven by internal waves and also provide valuable information about the possible remote consequences of internal wave generation.

3. Data and Methods

Super Typhoon Mangkhut originated on September 7 of 2018 as a tropical depression in the Central Pacific Ocean. It later moved westward into the Philippine Sea, where it intensified considerably until the TC's maximum 1-minute wind speeds stayed above 70 m s^{-1} (category 5) for almost four days (Fig. 1). As described by Johnston et al. (2020), an array of eight SOLO II profiling floats (Davis et al. 2001) sampled the upper $\sim 180 \text{ m}$ of the ocean under Mangkhut's tempestuous winds (Fig. 3.a). While Johnston et al. (2020) used this dataset to study the changing ocean stratification under a sequence of cyclones and possible implications for TC-TC interactions, the present analysis only uses measurements obtained beneath Super Typhoon Mangkhut (Figs. 1.b, 3).

Upon deployment, our floats modified their buoyancy to dive below 180 m depth and back to the surface at $\sim 35 \text{ min}$ intervals. While doing so, they sampled profiles of T and S in the upper ocean and drifted with the depth-varying currents. Because SOLO II floats record their coordinates at the beginning and end of every dive cycle, their geolocation data allows to produce two estimates of horizontal velocity. Surface estimates \mathbf{u}_{surf} , which are subject to wave motion and windage, are calculated using the drift between consecutive dives, when floats remain at the surface and transfer data via satellite. Meanwhile, we calculate \mathbf{u}_{mean} using the difference between the start and end locations of individual dives; thus, \mathbf{u}_{mean} represents a weighted average of depth-varying currents between the surface and the total depth $H > 180 \text{ m}$ of profiles.

On September 12, when the storm's maximum winds were above 70 m s^{-1} , and after the floats had moved westward with the North Equatorial Current, Super Typhoon Mangkhut swept over this region and its eye came within 250 km or less from six of our floats (Fig. 1, Johnston

et al. (2020)). To understand variations in the measurements made by different floats, we linearly interpolated JTWC best track data for Mangkhut to the times of each sampled profile and then referenced float data onto storm-following coordinates (Fig. 3.b).

In what follows, along-track and cross-track coordinates are represented by x and y respectively. Similarly, horizontal ocean velocities u, v are defined in these directions. Note that positive values of x denote regions behind the storm eye, while $y > 0$ indicates locations right of Mangkhut's track. Likewise, the time axis in our visualizations uses the storm's mean sampled speed $U_{storm} = 6.2 \text{ m s}^{-1}$ to transform along-track distances into time as $U_{storm}t = x$. Our plots show time scaled in terms of inertial periods as $t \frac{f}{2\pi}$. While Mangkhut moved from 13.7°N to 17.4° during our sampling period (Fig. 1), we use f at 15.54°N for convenience, as it produces the correspondence $U_{storm} \frac{2\pi}{f} = 1000 \text{ km}$ (Fig. 3.b).

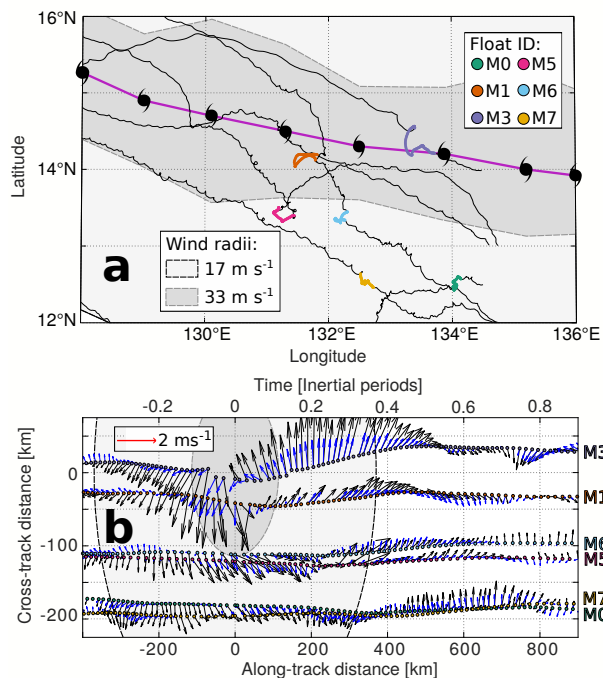


FIG. 3. Experiment overview: Panel **a** shows 6-hourly data locating Super Typhoon Mangkhut in the Western North Pacific Ocean during September of 2018 (purple). Black lines mark the trajectories of SOLO II floats, while vertical profiles used in this study are highlighted in colors. Panel **b** shows the distribution of float measurements in storm-following coordinates. Black (blue) vectors correspond to observed surface (depth-averaged) velocities.

Because our floats were deployed neither simultaneously nor perpendicular to the storm track, measurements that appear at the same along-track position in Figure 3.b in fact represent different points in time and can be separated by as much as 14 hours. Despite the fact that each float

effectively sampled the storm at a different time, the spatial distribution of sampled velocities in Figure 3.b line up to form a large vortex that mirrors the cyclonic winds. The circulation described by our instruments resembles historical results from numerical and observational studies alike (Chang and Anthes 1978; Price 1981; Price et al. 1994; Chang et al. 2013).

Considering the space-time transformation used to reference float data in this coordinate system, our velocity measurements (Fig. 3.b) suggest that the ocean response to Mangkhut was quasi-stationary in a storm-following frame of reference. Linear theory indicates that this can happen when storm characteristics are constant in time (Geisler 1970). Accordingly, wind speed data in Figure 1 confirm that Mangkhut's intensity was relatively unchanged, with maximum winds above 70 m s^{-1} , while we sampled the ocean around it.

a. 3D reconstruction of the ocean response

To best exploit the spatial information embedded within our dataset, we used objective mapping (Davis 1985) with a Gaussian decorrelation scale of 150 km to horizontally interpolate data sampled at each depth and generate continuous fields of temperature, salinity and horizontal currents. Stacking our two-dimensional maps on top of each other, we produce interpolated 3D fields T^*, S^*, u^*, v^* that are analyzed in the coming sections. Henceforth, the star $*$ indicates that a variable has been interpolated through objective mapping.

As mentioned above, float data include two velocity estimates $\mathbf{u}_{surf}, \mathbf{u}_{mean}$. Our analysis uses these two measurements and the mixed layer depth h to recreate a plausible flow structure (Eq. 13). Namely, we assume that the depth-dependence of wind-forced currents can be described by two layers of constant velocity and a sheared transition layer between them

$$\mathbf{u}^*(x, y, z) = \begin{cases} \mathbf{u}_{surf}^* & z \geq -h \\ \mathbf{u}_{surf}^* + \left\langle \frac{\partial \mathbf{u}}{\partial z} \right\rangle (z - h) & -h > z > -h - l \\ \mathbf{u}_{surf}^* + \left\langle \frac{\partial \mathbf{u}}{\partial z} \right\rangle l & -h - l \geq z \geq -H \end{cases} \quad (13)$$

Flow in the uppermost layer, which spans the depth of the mixed layer $-h < z \leq 0$, is given by \mathbf{u}_{surf}^* . Here, the thickness h of the mixed layer is defined as the depth at which T^* is 0.2°C colder than it is at 20 m depth. Below $z = -h$, we assume a transition layer of thickness $l = 30 \text{ m}$ (Johnston and Rudnick 2009) and constant shear

$$\left\langle \frac{\partial \mathbf{u}}{\partial z} \right\rangle = 2H \frac{\mathbf{u}_{surf}^* - \mathbf{u}_{mean}^*}{[l^2 + 2l(H - l - h)]}. \quad (14)$$

The third and deepest layer has a velocity $\mathbf{u}_{surf}^* + \left\langle \frac{\partial \mathbf{u}}{\partial z} \right\rangle l$ and extends down to the cast depth $H = 180 \text{ m}$. Equation

(14) defines the vertical shear $\langle \frac{\partial \mathbf{u}}{\partial z} \rangle$ so that the vertical average of resulting velocity profiles (Eq. 13) yields \mathbf{u}_{mean}^* . Lastly, we imposed a condition of adiabatic continuity to obtain vertical gradients $\frac{\partial w^*}{\partial z} = -\frac{\partial u}{\partial x} - \frac{\partial v}{\partial y}$. Assuming a rigid lid so that $w^*(z=0)$ vanishes, we infer vertical profiles $w^*(z)$ at a given point (x, y) as

$$w^*(z) = \int_0^z \left(\frac{\partial u^*}{\partial x} + \frac{\partial v^*}{\partial y} \right) dz'. \quad (15)$$

Note that, because $\mathbf{u} = (u, v)$ is constant within the mixed layer, so is its divergence. This means that Equations (7, 10, 15) are equivalent within the mixed layer in the absence of turbulent entrainment. Although turbulence and mixing are expected to be extraordinarily high under a typhoon, we assume that their impacts to the density of seawater are not large enough to drastically affect continuity, so that Equation (15) provides a physically sound estimate of w in the ocean interior.

The 3D fields $T^*, S^*, \mathbf{u}^*, w^*$ obtained using the methods outlined above are presented in the next sections. To analyze the impacts of precipitation in near-surface measurements of S and T , we interpolated data from the Integrated Multi-Satellite Retrievals for GPM (IMERG, Huffman et al. (2015)) onto the locations of our floats. Section 4 uses the near-surface fields $T^*(x, y, z=0)$, $S^*(x, y, z=0)$ (produced with data averaged between 0.5 and 1.5 m depth) to discuss the roles of diffusion and air-sea fluxes in Equations 1 & 2, while Section 5 describes u^* and v^* . Vertical motions, their role in the generation of internal waves and implications to the heat budget in Equation (1) are discussed in Section 6. A discussion of our findings follows in Section 7 while our conclusions are laid out in Section 8.

4. Near-surface thermodynamics

a. Mixed layer deepening and turbulent entrainment

Space-time variations in T and S under the sea surface result from processes in Equations (1) and (2). In the case of intense, fast-moving TCs like Mangkhut, shear-driven mixing at the base of the mixed layer is expected to cool the upper ocean at a rate much higher than Q_{atm} (D'Asaro 2003; Vincent et al. 2012a). This process is evidenced by SST measurements (T data averaged between 0.5 and 1.5 m depth) made by our floats (Fig. 4.a), all of which show cooling trends during storm passage. In particular, 1-m binned profiles of T , S and potential density σ_0 taken by float M3 show a clear, gradual deepening of the mixed layer in the 250 km ahead of the storm's eye (Figs. 4.b-d).

Because profiles in Figures 4.b-d show decreases in SST, but increases in both sea surface salinity (SSS) and density, the observed deepening of the mixed layer indicates the entrainment of cold, salty water from below. As further

evidence of the vigorous turbulence that transformed ocean thermodynamics beneath Mangkhut, many density profiles in Figure 4.d feature large regions with unstable stratification. These regions, known as unstable overturns, are a precursor to turbulence in stratified fluids whose contribution to vertical mixing depends on overturn size and the background stratification (Thorpe 1977; Thompson et al. 2007). Section 6 shows estimates of the turbulent diffusivity κ within these overturns.

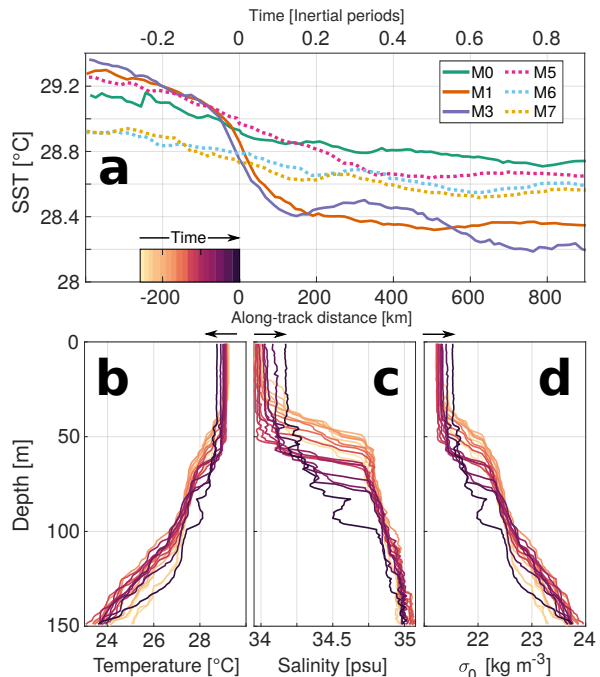


FIG. 4. Sea surface temperature (SST) measured by all floats is shown as a function of along-track distance in panel a. 1-m binned profiles of temperature (b), salinity (c) and density (d) measured by float M3 show the mixed layer deepening. Individual profiles shown in the lower panels are coded by their corresponding along-track distance as shown in panel a.

Measurements in Figure 4 show the effects of cold, salty water entrained upward into the mixed layer. However, SSS data in Figure 5.a show clear influence of precipitation, as floats M5, M6 and M7 sampled sharp decreases in SSS between 150 km and 250 km ahead of Mangkhut.

To explain this, IMERG data in Figure 5.b represent the hourly rate of precipitation (size of circles) and its accumulation (color of circles). Notice that all floats experienced significant rainfall; however, SSS did not decrease significantly for M1 and M3, which encountered the most precipitation (Fig. 5.b).

The development and growth of stable near-surface rain layers depends on the rate at which turbulence mixes freshwater and buoyancy production by rainfall (Eq. 2). Thus,

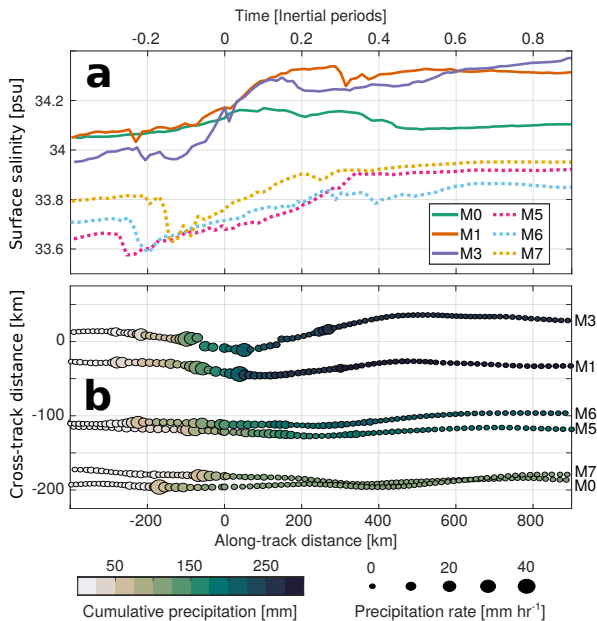


FIG. 5. SSS, calculated as a 5-meter average along the float tracks in panel a. IMERG datashow the precipitation rates and cumulative rainfall experienced by each float in panel b. As expected, greater values of time-averaged precipitation appear closer to the typhoon eye.

rain layers cannot be sustained when wind speeds (and the corresponding near-surface turbulence) are above a threshold value determined by the instantaneous precipitation rate (Thompson et al. 2019). Because our float measurements were made in intervals of roughly 35 min, salinity anomalies that persist over three or more consecutive profiles (rain layer duration > 70 min) are rare. Nonetheless, data retrieved by float M7 in the upper 30 m of the ocean show the detailed evolution and destruction of a rain layer (Fig. 6).

Vertical profiles in Figures 6.c-e show that the large negative salinity anomaly that is evident in M7’s surface measurements (Fig. 5.a) was initially confined to the upper 10 m but later diffused downward over the following 5 casts (Fig. 6.d). Correspondingly, temperature profiles show freshwater as a cold shallow anomaly that gradually deepens and is eventually overcome by vertical mixing of colder, salty water from below (Fig. 6.c). As higher wind speeds cause greater levels of turbulence in the upper ocean, the lifespan of rain layers shortens and their detection becomes less likely (Thompson et al. 2019). Thus, it is likely that floats M1 and M3 did not measure significant SSS freshening (Fig. 5.a) because of the increased wind speeds and corresponding shear-driven turbulence that occur near the storm track Price (1981).

In accordance with previous measurements and numerical simulations (Price 1981; D’Asaro et al. 2007; Sanford et al. 2007), changes in SST beneath Mangkhut display a

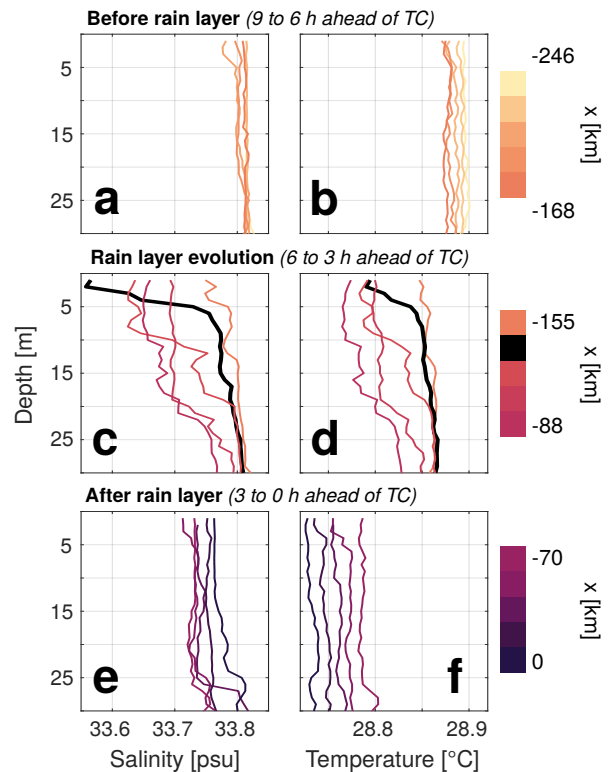


FIG. 6. Evolution of a rain layer in three stages. Each row of subfigures shows data from 5 consecutive profiles (color-coded by along-track position x) taken over a ~ 3 h period. The upper panel shows vertical profiles of S (a) and T (b) measured by float M7 before SSS was significantly affected. The middle panel shows a rapid decrease in near-surface salinity (c) and temperature (d). Initially, freshwater anomalies were confined to the upper 5 m (black line), but were layer diffused across a greater depth (maroon lines). Lastly, turbulent mixing has mostly de-stratified the upper ocean in panels e and f.

strong gradient in the along-track direction (Fig. 7.a). Correspondingly, the maximum cooling rate of SST was observed within 100 km of Mangkhut’s eye, while the greatest anomalies occurred within a narrow wake of increased SSS that leans towards the right side of the storm track in Figure 7.b. Although our floats preferentially sampled the left side of the storm and interpolated fields can become unreliable beyond the edges of our sampling area, measurements from floats M1 and M3 offer nearly symmetric coverage of near-surface conditions on both sides of the storm track (Fig. 3.b). Because the decrease in SST cooling measured by float M3 was consistently greater (Fig. 4.a), the rightward bias that is apparent in the shape and location of the cool, salty wake in Figure 7 suggests a rightward bias caused by the asymmetric distribution of windwork and shear-driven mixing (Chang and Anthes 1978; Price 1981). In summary, changes in T and S observed under Mangkhut are consistent with the entrainment of cold, salty waters across

the mixed layer base as the dominant mechanism for SST cooling under high-intensity storms Vincent et al. (2012a).

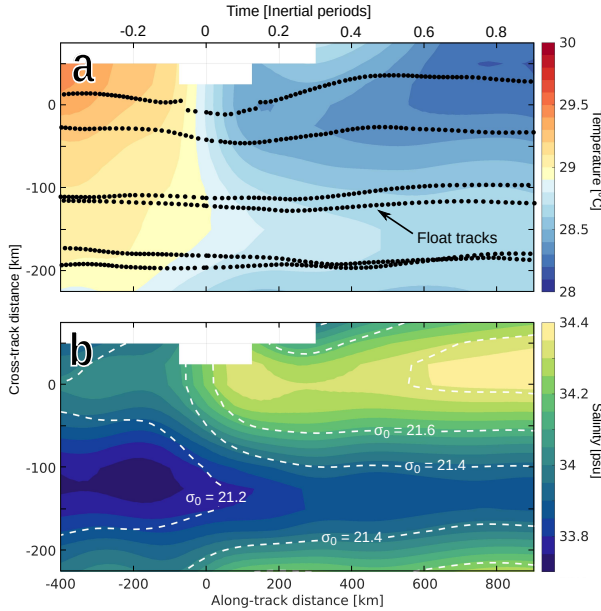


FIG. 7. Interpolated values of T (a) and S (b) averaged over 5 m below the ocean surface. Black dots in panel a show the locations of float measurements, while dashed contours in (b) show values of potential density σ_0 [kg m^{-3}].

b. Turbulent ocean heat pump

While TC-driven turbulence is best known for its impact on SST (Fig. 7.a) and subsequent implications to air-sea heat fluxes, TCs also leave a long-lasting signature on upper ocean thermodynamics, as recently revisited by Johnston et al. (2020). Many studies have explored these long-term processes and their potential contribution to shape ocean circulation in the tropics (Emanuel 2001; Srivier and Huber 2007; Jansen and Ferrari 2009; Mei et al. 2013). However, quantifying the amount of heat transported into the ocean interior by TC-driven motions often requires making assumptions about the magnitude, extent, and persistence of anomalous κ (Srivier and Huber 2007; Jansen et al. 2010; Fedorov et al. 2010). Empirical analyses of ocean mixing beneath TCs can thus provide insight into the duration and intensity of turbulent heat fluxes into the deeper ocean that are crucial to understand the long-term contributions of TCs to shape global climate (Emanuel 2001).

Temporal changes in T-S relationships can inform the vertical extent of turbulent ocean mixing (Hautala et al. 1996; Alford et al. 1999; Moum et al. 2003). However, our measurements are neither Eulerian nor Lagrangian, so T-S relations in our data result from combinations of turbulent,

advective, and atmospheric processes (Eqs. 1 and 2). Fortunately, turbulence and advection can be differentiated by their characteristic effects on T-S plots (Hautala et al. 1996; Talley 2011), as shown by data retrieved by floats M1 and M3 (Fig. 8).

The progression of water-mass properties measured by floats M1 and M3 throughout 200-km-long segments is color-coded in Figure 8.a. By comparing the time-averaged T-S properties sampled at different stages of storm passage, we seek to infer the processes responsible for observed transformations. For example, average profiles measured by float M3 within the range $200 \leq x \leq 400$ km (dashed blue line) are compared to data from $400 \leq x \leq 600$ km (solid line) in Figure 8.b.

In order to determine the extent to which turbulence-enhanced mixing may have shaped the transition between observed profiles in Figure 8.b, we used the mean profiles from 200-400 km to initialize a diffusive model with depth-constant κ that would approximate vertical profiles in 400-600 km in the absence of advection (Eqs. 1, 2). T-S properties that result from applying $\kappa = 3 \times 10^{-3}$ and $1 \times 10^{-2} \text{ m}^2 \text{ s}^{-1}$ over a 9 h period (0.2 inertial periods at 15.54°N) are shown with black dashed lines in Figure 8.b. Modelled profiles of T and S agree well with observed changes (Fig. 8.b) and show that vertical mixing can explain T-S transformations for $\sigma_0 < 23.2 \text{ kg m}^{-3}$. Vertical diffusivities $\kappa \sim 1 \times 10^{-2} \text{ m}^2 \text{ s}^{-1}$ agree with Thorpe scale estimates shown in Section 6 and suggest mixing as the dominant process in water-mass transformations down to ~ 110 m depth at least 400 km behind Mangkhut's eye.

T-S profiles in Figure 8.b feature an increase in salinity for $\sigma_0 > 23.5 \text{ kg m}^{-3}$. Modelled solutions (dashed lines in Fig. 8.b) show that such a transformation cannot result from mixing alone, and thus we attribute it to horizontal advection. Namely, vertical mixing was the primary process responsible for sampled water-mass transformations down to 110 m depth, while advection made more significant contributions at greater depths.

5. Upper ocean motions

Interpolated fields \mathbf{u}_{surf}^* and \mathbf{u}_{mean}^* show a strong cyclonic circulation that mirrors the structure of TC winds (Fig. 9). For both velocity fields, speed is greater near the right side of the storm (positive cross-track distance y) and reaches a minimum value roughly 50 km behind and left of the typhoon eye (Figs. 9.a,b). Although objectively mapped variables can become unreliable near the edges of our sampling area, a comparison between velocities measured by floats M1 and M3 on both sides of the storm track (Fig. 3.b) shows that speeds observed in the wake of Mangkhut were in fact greater for $y > 0$ than $y < 0$. Consistent with the asymmetric cold, salty wake in Figure

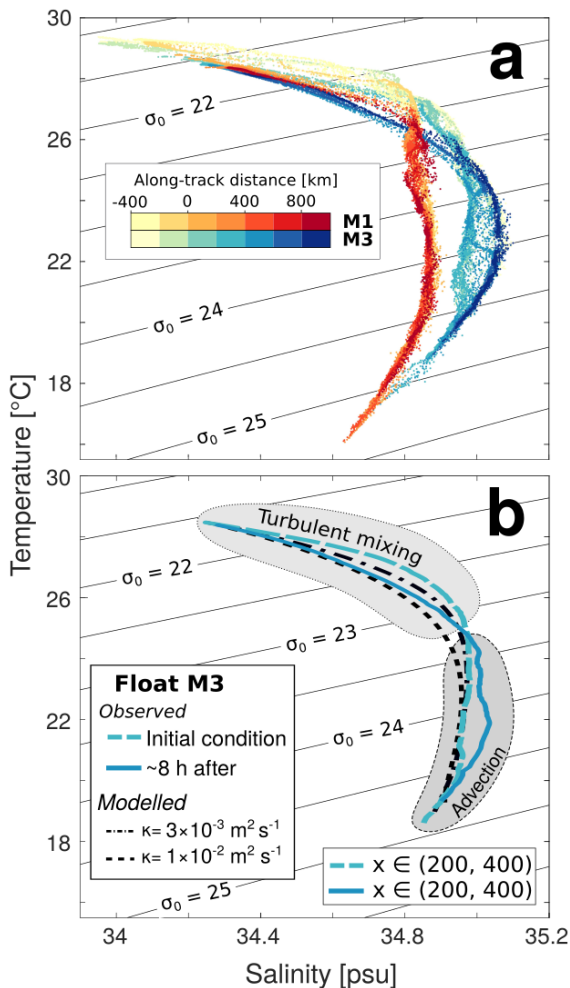


FIG. 8. T-S profiles measured by floats M1 and M3 are color-coded by along-track distance in panel a. Mean profiles measured between 200 and 400 km (Before, dashed line) and between 400 and 600 km (After, solid line) in panel b show the cumulative transformations caused throughout an 8 h period, while black dashed lines show T-S properties modelled using a diffusion model with depth-constant diffusivities $\kappa = 3 \times 10^{-3}$ and $1 \times 10^{-2} \text{ m}^2 \text{ s}^{-1}$.

7, this pattern indicates a higher rate of wind-ocean energy transfer on the right side of the storm track (Chang and Anthes 1978; Price 1981; Zedler 2009) and resembles composite maps of surface velocity under historical TCs (Chang et al. 2013, 2016).

Because turbulence under TCs is primarily driven by vertical shear at the bottom of the mixed layer Price (1981), the difference $\mathbf{u}_{surf}^* - \mathbf{u}_{mean}^*$ is a proxy for the spatial distribution of turbulent fluxes across the mixed layer bottom (Fig. 10.a). Spatial patterns in $\mathbf{u}_{surf}^* - \mathbf{u}_{mean}^*$ are consistent with the suppression of kinetic energy in the left side of the storm and the rightward cooling bias (Figs. 7, 9, Chang and Anthes (1978); Price (1981)). In turn, Figure

9.b shows the vertical flow structure (Eqs. 13-15) produced by $\langle \frac{\partial \mathbf{u}}{\partial z} \rangle$ suggests a lag between flow in the mixed layer and below. For a better understanding of baroclinic motions beneath Mangkhut, we now examine mapped patterns in Γ and their relation to w^* (Eq. 15).

Knowing that our estimates (Fig. 9) of ocean velocities under Mangkhut agree with known theory, we separate velocity fields into their vortical and divergent components to diagnose vertical displacements below the ocean surface as described in Equations (8)-(10). This vorticity-divergence (ζ, Γ) view of upper ocean motions beneath Mangkhut is dominated by a high-vorticity core (color shading in Figures 9.c,d) that reaches values as high as $\zeta/f \sim 1$ for \mathbf{u}_{surf}^* (Fig. 9.c) and $\zeta/f \sim 0.4$ for \mathbf{u}_{mean}^* (Fig. 9.d). This maximum in ζ/f corresponds to the ocean's immediate response to tangential winds (Eq. 8) under fast-moving storms.

As wind gradients weaken away from the typhoon's maximum wind radius (MWR) and ζ, Γ evolve freely (Eqs. 11 & 12), the wind-forced ζ/f evolves into Γ/f (noted by black contours in Figs. 9.c,d) and reaches peak values of $\Gamma/f \sim 0.7$ roughly 150 km behind (~ 0.15 inertial periods after) the vorticity maximum. Farther behind, at $x = 450$ km, an area with $\zeta/f < 0$ emerges from the waning divergence, suggesting that ζ and Γ are coupled in waves by the inertial oscillation of wind-powered currents (Eqs. 8-10 and Fig. 2).

To better understand the space-time patterns observed in ζ and Γ , we computed numerical solutions of the mixed layer model in Equations (8)-(10) under idealized TC-like atmospheric forcing (Fig. 11). In our diagnostic model, Mangkhut is represented by two Gaussian curves (Fig. 11.a) that quantify the vorticity of tangential stresses ($\nabla \times \tau$, black line) and the convergence of low-level winds ($\nabla \cdot \tau$, gray line) around the typhoon eye. Because our goal here is to test the validity of the (ζ, Γ) framework, we compare our reproduction of Mangkhut's winds to the mean vorticity $\frac{|\tau_{max}|}{MWR}$ of TC wind stresses (Fig. 11.a). The maximum wind stress $|\tau_{max}| = C_D \rho_{air} |U_{10}|^2$ (dashed line, Fig. 11.a) was calculated using $C_D \rho_{air} \sim 1.5 \times 10^{-3} \text{ kg m}^{-3}$ (Powell et al. 2003), while the maximum wind speed $U_{10} = 70 \text{ m s}^{-1}$ and MWR = 40 km were based on JTWC data. Despite the simplicity of our representation of TC winds, solutions of Equations (8)-(10) under the imposed forcing and a damping rate $r = 0.5f$ agree well with observations of surface currents (Fig. 11.b) and isothermal displacement (Fig. 11.c) along the storm track.

As described in Section 2 and confirmed with observations in Figure 11, tangential winds drive a cyclonic circulation in the upper ocean that peaks shortly behind the storm eye. Next, as the Coriolis force steered currents in clockwise near-inertial rotation, vortical flow patterns

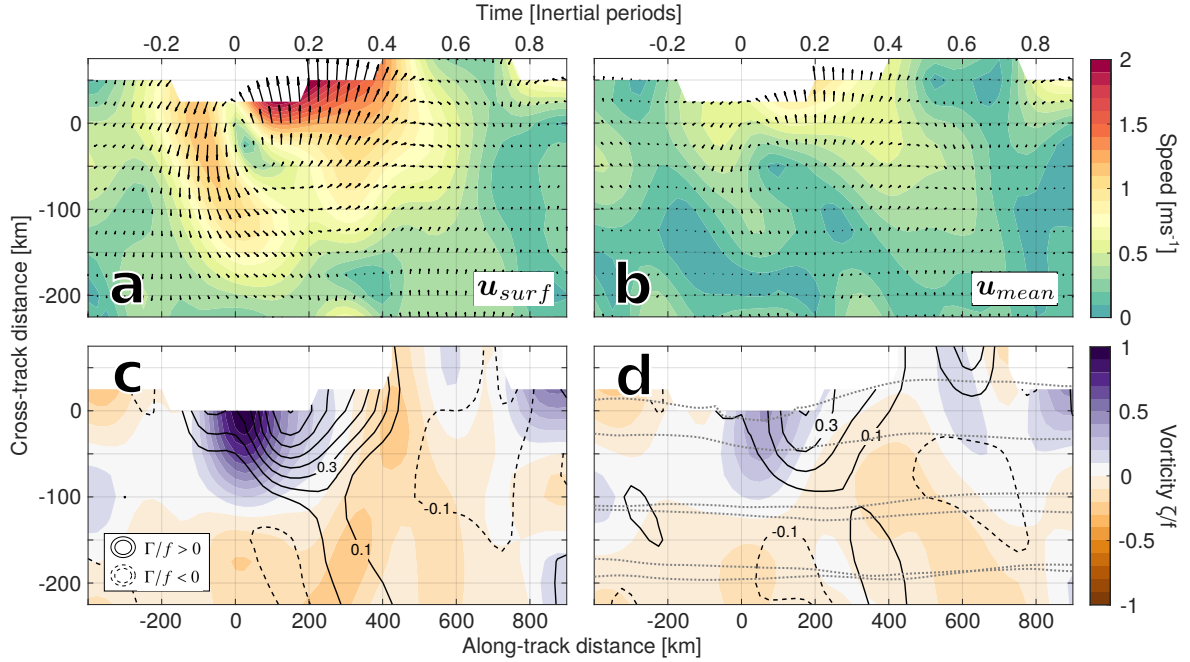


FIG. 9. Two-dimensional maps of \mathbf{u}_{surf} (left) and \mathbf{u}_{mean} (right) are viewed through their speed and direction (a, b) and their vortical-divergent components (c, d). Color in c,d shows ζ/f of the surface (left) and depth-mean (right) flows, while Γ/f is shown in black contours. Contours of Γ are shown at 0.1 intervals and are continuous for upwelling-favorable regions ($\Gamma > 0$), while dashed contours show downwelling-favorable convergence ($\Gamma < 0$). Dotted lines in (d) show the float tracks.

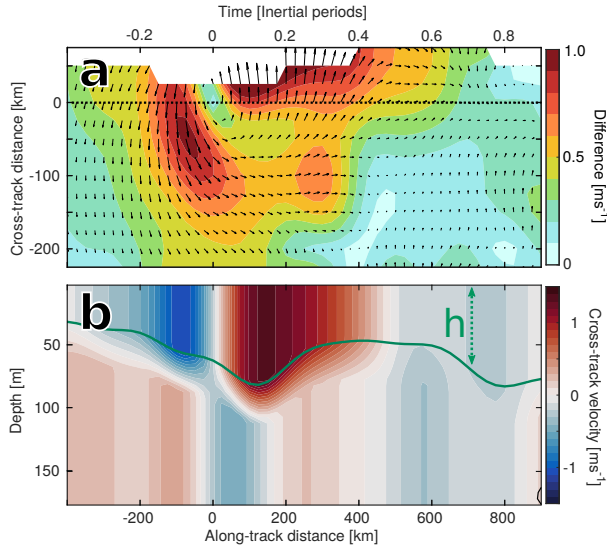


FIG. 10. The direction (arrows) and magnitude (color shading) of differences $\mathbf{u}_{surf}^* - \mathbf{u}_{mean}^*$ used to estimate $\left\langle \frac{\partial \mathbf{u}}{\partial z} \right\rangle$ (Eq. 14) are shown in panel a. Color shading in panel b shows vertical profiles (Eq. 13) of cross-track velocity $v(x, y=0, z)$ inferred along the storm track (dotted line in a). The green line in b indicates the mixed layer depth h , which defines the upper layer in our three-layer velocity profiles (Eq. 13).

were rearranged to become divergent. At this point, divergent surface flows behind the storm would presumably drive upward motions in the ocean interior (Eq. 10), as confirmed by vertical profiles of T^* in Figure 12.

Observations in Figure 11.c show that, after an initial stage where mixing deepens the mixed layer, numerical solutions of upwelling (solid line) reproduce vertical motions of the 27°C isotherm (dashed line, Fig. 11.c). Observations show that the 27°C isotherm deepened by ~ 25 m under the typhoon eye before it traveled up 70 m as predicted by model solutions. Although the simple numerical solutions in Figure 11 ignore the effects of mixing of momentum, our results suggest that simple models of mixed layer dynamics can help diagnose early near-inertial disturbances of the ocean stratification that later evolve into NIW wakes. However, note that the validity of linear dynamics in the wake of TCs is lost gradually as nonlinear interactions between near-inertial currents and vertical shear generate higher-frequency waves D'asaro (1995); Niwa and Hibiya (1997).

6. Generation of the internal wave wake

As suggested by surface velocity data in Figure 9 and numerical solutions in Figure 11, horizontal divergence in the wake of Mangkhut produced upward motions in the form of an upwelling jet that lifted cold, deep water towards

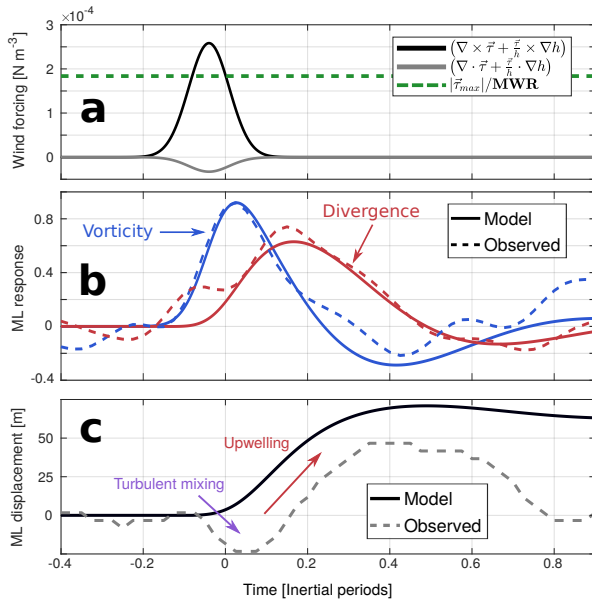


FIG. 11. Mixed layer response to idealized TC-like atmospheric forcing. Numerical solutions of Equations (8)-(10) were obtained using the wind forcing terms shown in panel **a** and compared in **b** to estimates of ζ/f (blue) and Γ/f (red) made using \mathbf{u}_{surf}^* (Fig. 9.c) along the storm track. Upwelling in model solutions of $h(t)$ agrees well with observed displacements of the 27 °C isotherm (**c**).

the ocean surface (Fig. 12). Inferred profiles of w^* and v^* (vectors in Fig. 12.a, w^* magnified to reveal areas of upwelling) reveal the structure of this flow, in which w^* reached 8 m h⁻¹. Ultimately, the upwelling jet in Figure 12.a lifted isotherms by as much as 75 m nearly 400 km (~ 0.4 inertial periods) behind the typhoon eye. It is worth noting that regions with $\Gamma/f < 0$ must have occurred well below 180 m depth in order to supply the cold ($T < 20$ °C) water that makes up the NIW in Figure 12.a.

Farther behind the typhoon, at $x=700$ km, isotherms ascended to positions ~ 20 m higher than they occupied ahead of the upwelling jet (Figs. 11.c, 12.a). This suggests that ocean stratification along the storm track was modified by both mixing and net upwelling. Static overturns measured by float M3 were processed to calculate turbulent diffusivities κ following the method in Thompson et al. (2007). Results are shown in Figure 12.b, where the vertical extent of instabilities and the associated turbulence-enhanced κ is overplotted in purple. Notably, density overturns appeared in virtually every profile taken between $x = -150$ and $x = 150$ km by float M3, consistent with the rapid rate of SST cooling observed near the TC eye (Figs. 4, 7).

To test the impacts of advection in setting the ocean stratification behind Mangkhut, as well as the accuracy of inferred 3D flows (Eqs. 13-15), Figure 12.b shows the Eulerian heating rate $\frac{\partial H_c}{\partial t} = \rho_0 C_p \frac{\partial T^*}{\partial t}$ calculated along the

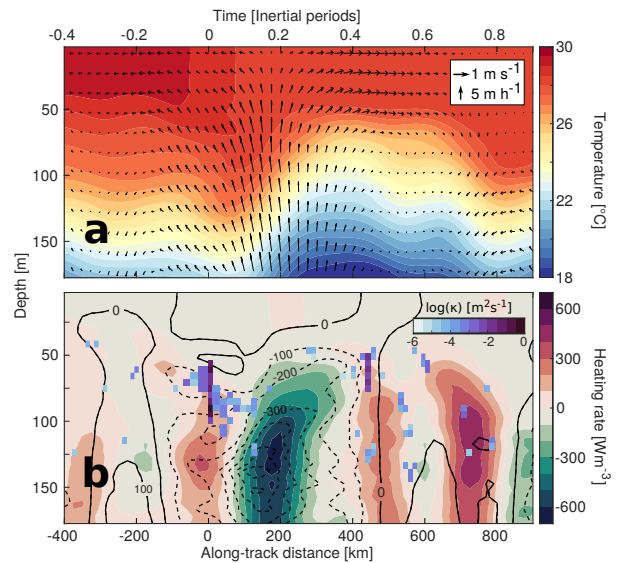


FIG. 12. Vertical sections of temperature and (u, w) velocities in panel **a** show the generation of an internal wave wake behind Super Typhoon Mangkhut. The vertical component w of velocity vectors is magnified to highlight areas of upwelling and downwelling. Panel **b** shows an estimate of the Eulerian heating rate $\frac{\partial H_c}{\partial t} = U_{storm} \frac{\partial H_c}{\partial x}$ (color shading) and the contributions of advective terms in Equation (1) (black contours at 100 Wm⁻³ intervals, dashed for negative values).

storm track through two different methods. First, we calculated the along-track gradients $\frac{\partial T^*}{\partial x}$ and related them to the heating rate by a frozen field assumption $\frac{\partial T^*}{\partial t} = U_{storm} \frac{\partial T^*}{\partial x}$ (color shading). Second, we used the 3D currents (u, v, w) to calculate the advective component of Eulerian heating (black contours in Figure 12.b, first two terms in the right hand side of Equation (1)) below the storm track and compared it to the T,S-based estimate. Using T,S data and a weighted average of the storm's translating speed $U_{storm} = 6.2$ ms⁻¹, we calculated $\frac{\partial H_c}{\partial t} = U_{storm} \frac{\partial H_c}{\partial x}$ as shown by color shading in Figure 12.b. Agreement is qualitatively good between both estimates of subsurface heating and relatively accurate within the convective region centered 180 km behind the storm, where the local heating rate surpassed 600 Wm⁻³. Nevertheless, our flow field underestimates subsidence 700 km behind the storm and mistakenly predicts advective cooling deep below Mangkhut's eye, where observations (color shading) show heating rates as high as 300 Wm⁻³.

Disagreement between heating rates estimated directly below the typhoon eye (Fig. 12.b) may be explained by the vigorous mixing that deepened the mixed layer ahead of Mangkhut (Fig. 11.c). While the advective terms in Equation 1 predict significant ocean cooling below 70 m depth, estimated values of κ suggest the rapid diffusion of warm waters into the deeper ocean (Fig. 12.b). As a result, the thermocline warmed directly beneath Mangkhut's eye,

where SST cooled at the highest rate (Fig. 8.a). Lastly, the presence of Thorpe scale estimates $\kappa \sim 1 \times 10^{-2} \text{ m}^2 \text{ s}^{-1}$ as far as 450 km behind the storm support the analysis in Figure 8.b.

Figure 12 shows that the intensity of heat transfer processes is much greater at depth than it is near the ocean surface, which is shielded by the homogeneous thermodynamics of the mixed layer (Mei et al. 2015a). Knowing that clockwise, periodic oscillations of current vectors at the Coriolis frequency f allowed for the vertical motions described above, we now present evidence of the horizontal propagation of internal waves that result from patterns in ocean divergence Γ . We use the advective relations between Γ , w , and the ocean stratification N (Eqs. 1, 2, 15) to interpret data in Figure 13, which provide complementary views of internal wave properties behind Mangkhut.

Taken at 160 m depth, horizontal sections of ζ , Γ , and N shown in Figure 13 reveal the structure of internal waves in the wake of the storm. Spatiotemporal patterns in Γ and N are related by vertical flows (Eq. 15), which displace the ocean thermocline and thus change N in Figure 13.b.

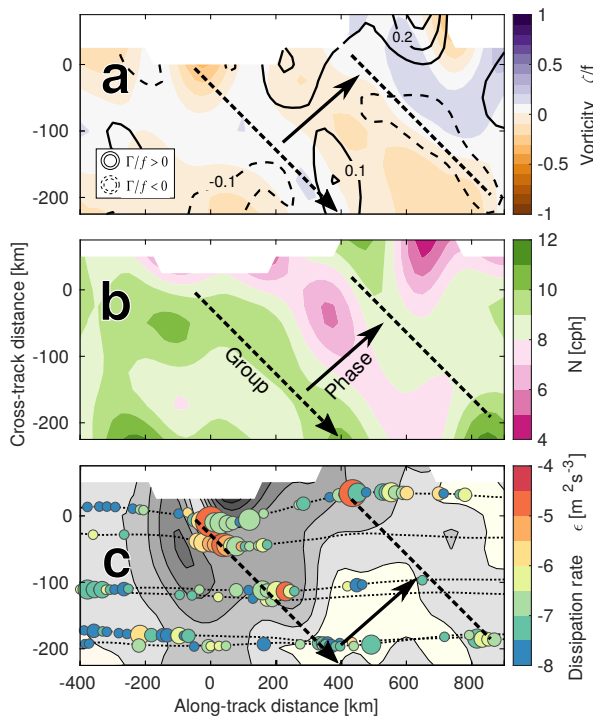


FIG. 13. Horizontal sections of vorticity and divergence (a), and the buoyancy frequency (b) at 160 m depth show the spatial structure of internal waves in the wake of Mangkhut. The color of circles in panel c show depth-averaged estimates of the dissipation rate ϵ , while their size indicates the height of overturns (range is between 5 and 25 m). Gray shading in (c) is reproduced from Fig. 10.a and represents the magnitude of vertical shear below the mixed layer, while dotted lines in denote individual float tracks.

A plan view of Thorpe scale estimates of turbulence (Fig. 13.c) shows that most mixing occurs in areas of high shear ahead of the storm D'Asaro (2003). Furthermore, the spatial distribution of overturns provides further information about the propagation of internal waves. Starting near the typhoon eye, all 6 of our floats sampled a narrow front of static overturns that propagated away from the storm track with speed $\sim 3.1 \text{ ms}^{-1}$ (dashed lines in Fig. 13). Half of an inertial period later, three floats measured a similar streak of enhanced turbulence extending between $(x = 450, y = 25)$ and $(x = 900, y = -200)$. Given the similarities between these patterns and lines of equal phase in Figures 13.a,b, the diagonal tracks of turbulence in Figure 13.c suggest that ocean mixing moves away from TC tracks with the phase of super-inertial internal waves.

Numerical simulations by Niwa and Hibiya (1997) detail the cross-track propagation of internal waves in the wake of TCs; features in Figure 13 share notable similarities with their results. Here, the advection of shear by NIWs generates low-mode, super-inertial internal waves with frequencies $2f$ and $3f$ that can rapidly propagate into the deep ocean (Niwa and Hibiya 1997; Zedler 2009). While the along-track wavelength $\lambda_A \sim 450 \text{ km}$ of features in Figure 13 corresponds to a frequency $\omega = U_{storm} \frac{2\pi}{\lambda_A} = 2.2f$, the measurements presented here cannot provide accurate estimates of wave frequencies. Likewise, higher-frequency motions are masked by the decorrelation scale (150 km) of our interpolated fields.

7. Discussion

Mixing is perhaps the most critical aspect of the ocean's response to TC forcing, because the entrainment of cold water upwards (Chang and Anthes 1978; Price 1981) cools the ocean surface and deepens the mixed layer. This process affects storm development (Schade and Emanuel 1999; Emanuel 1999; Balaguru et al. 2012) and in the long-term may increase the ocean's capacity for heat uptake (Emanuel 2001; Jansen et al. 2010; Mei et al. 2013). Measured profiles of T and S (Figs. 4.b-c & 8) and interpolated thermodynamical fields (Fig. 7) provide direct evidence of this process beneath a Super Typhoon, while static overturns in our record (Figs. 4.d, 12.b, 13.c) give a quantitative proxy for its significance.

By formulating a simple linear model of mixed layer dynamics (Eqs. 5-7) in terms of vorticity and divergence (Eqs. 8-10), we obtain new insight about the nature of vertical oceanic motions beneath and behind TCs. In particular we demonstrate that, in the wake of the storm, the cyclonic flow powered by Mangkhut's winds (Figs. 9) was rearranged by the Coriolis force so that its vorticity ζ was transformed into divergence Γ (Fig. 11, Eqs. 8 & 9). This led to the generation of a large NIW in the wake of Mangkhut (Fig. 12). Although this simple, one-dimensional representation of the ocean response to TCs

cannot reproduce complex processes that impact surface cooling (Yablonsky and Ginis 2009), it accurately predicted the location and magnitude of upwelling behind Mangkhut (Figs. 11, 12). Ultimately, this suggests that the generation of upwelling and NIWs under TCs is proportional to the vorticity of wind stress inside the storm eye, which can be approximated using the storm’s maximum wind speed U_{max} as U_{max}^2/MRW .

Because their frequency is low, NIWs propagate along nearly-horizontal rays and drive relatively small vertical displacements in the ocean interior (Alford et al. 2016). Yet, the internal wave generated by Mangkhut spanned roughly 75 m crest-to-trough, greater than previous observations of TC-generated and internal waves Price et al. (1994); Sanford et al. (2011); Guan et al. (2014).

While convergent-divergent patterns were most evident along the storm track (Fig. 9), horizontal sections of vorticity ζ and divergence Γ below the mixed layer show super-inertial internal waves propagating in the cross-track direction (Fig. 13). Here, independent estimates of subsurface vorticity ζ , divergence Γ , stratification N and turbulent dissipation ϵ reveal the structure of internal waves in the wake of Mangkhut. Although observations have shown the modulation of ocean mixing by the phase of internal waves before (Moum et al. 2003), the generation of phase-locked turbulent fronts within TC wakes (Fig. 13.c) had not been reported previously. As proposed by Niwa and Hibiya (1997), this result supports the role of super-inertial internal waves as efficient vehicles for remote, wind-driven mixing in the deep ocean (Cuypers et al. 2013).

The timescale $r^{-1} \sim 14.5$ h inferred for large-amplitude subsurface waves in this study is considerably lower than historical observations of mid-latitude storms, which usually range between 2 and 10 days (D’Asaro 1985). Similar to previous estimates of r^{-1} under TCs Guan et al. (2014), the increased rate of Eulerian momentum decay (D’asaro 1995) suggests TC-generated NIWs as more efficient vehicles for mixed layer motions to transfer their energy into the deep ocean. The contribution of wind-forced motions to the global internal wave budget is often calculated with reanalysis products (Alford 2001, 2003). However, rainfall in TCs can introduce considerable errors to satellite sensors of ocean winds that inform reanalysis products (Weissman et al. 2012). Furthermore, the spatial resolution of global wind datasets can fail to capture the intensity and spatial gradients of TC winds, (Walsh et al. 2007), thus underestimating the wind stress curl $\nabla \times \tau$ that drives NIW generation under these storms (Eqs. 8-10, Fig. 11).

8. Conclusions

We used data from an array of six autonomous profiling floats (Johnston et al. 2020) to reconstruct the 3D ocean response to Super Typhoon Mangkhut. Our analysis suggests

that SST cooling was dominated by the turbulent entrainment of cold, high salinity water into the mixed layer (Fig. 4), resulting in the formation of an asymmetric cold wake (Fig. 7). While the rightward bias in cooling is consistent with the expected distribution of windwork Chang and Anthes (1978); Price (1981) and momentum in the ocean mixed layer (Fig. 9), vertical profiles of density (Fig. 4.d) offer a direct description of the turbulent overturns (Figs. 12.b, 13.c) responsible for these thermodynamical transformations (section 6).

We use a simple diagnostic model (Eqs. 8, 9) to understand the evolution of observed mixed layer currents over time (Fig. 11) and the subsequent generation of a near-inertial internal wave (Figs. 10-13) as wind-forced vorticity is transformed into divergence by the Coriolis effect. Agreement between our observations and model simulations (Fig. 11) suggest that NIW generation under fast-moving TCs is primarily driven by the vorticity of wind stresses $\nabla \times \tau$ near the storm eye. Although we assumed that horizontal currents in the ocean interior follow a two-layer structure (Eqs. 13, 14), heat advection by our inferred currents is in good agreement with observations and dominated by vertical motions (Eq. 15) associated with the generation of NIWs (Fig. 12).

Direct observations with the spatial density and coverage achieved here (Fig. 3.b) are rare under storms as intense as Mangkhut. Measurements of this sort will likely continue to provide new insights about the wide breadth of ocean processes forced by TCs. This analysis aims to improve our understanding of internal wave generation behind tropical storms (Fig. 11), their subsequent propagation into the ocean interior and the resulting redistribution of heat and energy (Fig. 12). Aside from the well-known generation of NIWs, we find that static overturns sampled by our floats propagated away from the storm track with the phase of internal waves (Fig. 13).

Numerous questions remain about the distribution and temporal persistence of ocean turbulence powered by TCs and its role in shaping the global overturning circulation (Emanuel 2001; Sriviver and Huber 2007; Jansen et al. 2010; Mei et al. 2013; Cuypers et al. 2013). Watermass analyses in Figure 8 show that turbulent diffusivities $\kappa \sim 1 \times 10^{-2} \text{ m}^2 \text{ s}^{-1}$ can be sustained in the ocean thermocline even hundreds of kilometers behind a TC. Moreover, our study raises questions about the long-term fate of energy stored in wind-generated internal waves that propagate into the ocean interior, as the turbulent mixing associated with these waves (Figs. 12.a, 13.c) can modify ocean thermodynamics well below the permanent thermocline long after storm passage.

Data availability statement. Float data are available at the PISTON data site www-air.larc.nasa.gov/cgi-bin/ArcView/camp2ex?TRAJECTORY=1#JOHNSTON.

SHAUN. Tropical cyclone best track data are available from the JTWC at www.usno.navy.mil/NOOC/nmfc-ph/RSS/jtwc/best_tracks/index.html. MATLAB Scripts used to generate 3D maps of float data can be downloaded from github.com/inciente/PISTON/Mangkhut.

Acknowledgments. This work is supported by Grant NA17OAR4310259 from the Climate Variability and Predictability program at NOAA and N00014163085 from the Office of Naval Research's PISTON initiative, which are components of the international Years of the Maritime Continent program. We are grateful to the master, crew, and science party on *R/V Thomas Thompson* for their help in deploying floats. The Instrument Development Group at the Scripps Institution of Oceanography designed, prepared, and monitored the SOLO-II floats. E.J.T. contributes effort with funding from the NOAA Weather Program Office's Precipitation Prediction Grand Challenge. N.G.B. is funded by Consejo Nacional de Ciencia y Tecnología and UC Mexus. Kristin Zeiden provided valuable comments about our methods and the theory of internal waves.

References

- Alford, M. H., 2001: Internal swell generation: The spatial distribution of energy flux from the wind to mixed layer near-inertial motions. *Journal of Physical Oceanography*, **31** (8), 2359–2368.
- Alford, M. H., 2003: Improved global maps and 54-year history of wind-work on ocean inertial motions. *Geophysical Research Letters*, **30** (8).
- Alford, M. H., M. C. Gregg, and M. Ilyas, 1999: Diapycnal mixing in the Banda Sea: Results of the first microstructure measurements in the Indonesian Throughflow. *Geophysical Research Letters*, **26** (17), 2741–2744.
- Alford, M. H., J. A. MacKinnon, H. L. Simmons, and J. D. Nash, 2016: Near-inertial internal gravity waves in the ocean. *Annual review of marine science*, **8**, 95–123.
- Alford, M. H., and R. Pinkel, 2000: Observations of overturning in the thermocline: The context of ocean mixing. *Journal of Physical Oceanography*, **30** (5), 805–832.
- Asselin, O., and W. R. Young, 2020: Penetration of Wind-Generated Near-Inertial Waves into a Turbulent Ocean. *Journal of Physical Oceanography*, **50** (6), 1699–1716, doi:10.1175/JPO-D-19-0319.1, URL <https://doi.org/10.1175/JPO-D-19-0319.1>, <https://journals.ametsoc.org/jpo/article-pdf/50/6/1699/4950354/jpod190319.pdf>.
- Balaguru, K., P. Chang, R. Saravanan, L. R. Leung, Z. Xu, M. Li, and J.-S. Hsieh, 2012: Ocean barrier layers' effect on tropical cyclone intensification. *Proceedings of the National Academy of Sciences*, **109** (36), 14343–14347.
- Chang, S. W., and R. A. Anthes, 1978: Numerical simulations of the ocean's nonlinear, baroclinic response to translating hurricanes. *Journal of Physical Oceanography*, **8** (3), 468–480.
- Chang, Y.-C., G.-Y. Chen, R.-S. Tseng, L. R. Centurioni, and P. C. Chu, 2013: Observed near-surface flows under all tropical cyclone intensity levels using drifters in the northwestern Pacific. *Journal of Geophysical Research: Oceans*, **118** (5), 2367–2377.
- Chang, Y.-C., R.-S. Tseng, P. C. Chu, J.-M. Chen, and L. R. Centurioni, 2016: Observed strong currents under global tropical cyclones. *Journal of Marine Systems*, **159**, 33–40.
- Cuypers, Y., X. Le Vaillant, P. Bouruet-Aubertot, J. Vialard, and M. J. McPhaden, 2013: Tropical storm-induced near-inertial internal waves during the cirene experiment: Energy fluxes and impact on vertical mixing. *Journal of Geophysical Research: Oceans*, **118** (1), 358–380.
- D'Asaro, E. A., 1985: The energy flux from the wind to near-inertial motions in the surface mixed layer. *Journal of Physical Oceanography*, **15** (8), 1043–1059.
- D'Asaro, E. A., 1989: The decay of wind-forced mixed layer inertial oscillations due to the β effect. *Journal of Geophysical Research: Oceans*, **94** (C2), 2045–2056.
- D'asaro, E. A., 1995: Upper-ocean inertial currents forced by a strong storm. Part II: Modeling. *Journal of physical oceanography*, **25** (11), 2937–2952.
- D'Asaro, E. A., 2003: The ocean boundary layer below Hurricane Dennis. *Journal of Physical Oceanography*, **33** (3), 561–579.
- D'Asaro, E. A., T. B. Sanford, P. P. Niiler, and E. J. Terrill, 2007: Cold wake of hurricane Frances. *Geophysical Research Letters*, **34** (15).
- Davis, R., J. Sherman, and J. Dufour, 2001: Profiling ALACEs and other advances in autonomous subsurface floats. *Journal of atmospheric and oceanic technology*, **18** (6), 982–993.
- Davis, R. E., 1985: Objective mapping by least squares fitting. *Journal of Geophysical Research: Oceans*, **90** (C3), 4773–4777.
- Emanuel, K., 2001: Contribution of tropical cyclones to meridional heat transport by the oceans. *Journal of Geophysical Research: Atmospheres*, **106** (D14), 14771–14781.
- Emanuel, K. A., 1999: Thermodynamic control of hurricane intensity. *Nature*, **401** (6754), 665–669.
- Fedorov, A. V., C. M. Brierley, and K. Emanuel, 2010: Tropical cyclones and permanent El Niño in the early Pliocene epoch. *Nature*, **463** (7284), 1066–1070.
- Garrett, C., 2001: What is the “near-inertial” band and why is it different from the rest of the internal wave spectrum? *Journal of Physical Oceanography*, **31** (4), 962–971.
- Geisler, J. E., 1970: Linear theory of the response of a two layer ocean to a moving hurricane. *Geophysical and Astrophysical Fluid Dynamics*, **1** (1-2), 249–272.
- Gill, A., 1984: On the behavior of internal waves in the wakes of storms. *Journal of Physical Oceanography*, **14** (7), 1129–1151.
- Glenn, S., and Coauthors, 2016: Stratified coastal ocean interactions with tropical cyclones. *Nature communications*, **7** (1), 1–10.
- Guan, S., W. Zhao, J. Huthnance, J. Tian, and J. Wang, 2014: Observed upper ocean response to typhoon Megi (2010) in the Northern South China Sea. *Journal of Geophysical Research: Oceans*, **119** (5), 3134–3157.

- Hautala, S. L., J. L. Reid, and N. Bray, 1996: The distribution and mixing of Pacific water masses in the Indonesian Seas. *Journal of Geophysical Research: Oceans*, **101** (C5), 12 375–12 389.
- Huffman, G. J., D. T. Bolvin, D. Braithwaite, K. Hsu, R. Joyce, P. Xie, and S.-H. Yoo, 2015: NASA global precipitation measurement (GPM) integrated multi-satellite retrievals for GPM (IMERG). *Algorithm Theoretical Basis Document (ATBD) Version*, **4**, 26.
- Jaimes, B., and L. K. Shay, 2009: Mixed layer cooling in mesoscale oceanic eddies during Hurricanes Katrina and Rita. *Monthly Weather Review*, **137** (12), 4188–4207.
- Jansen, M., and R. Ferrari, 2009: Impact of the latitudinal distribution of tropical cyclones on ocean heat transport. *Geophysical Research Letters*, **36** (6).
- Jansen, M. F., R. Ferrari, and T. A. Mooring, 2010: Seasonal versus permanent thermocline warming by tropical cyclones. *Geophysical Research Letters*, **37** (3).
- Johnston, T. M. S., D. Chaudhuri, M. Mathur, D. L. Rudnick, D. Sengupta, H. L. Simmons, A. Tandon, and R. Venkatesan, 2016: Decay mechanisms of near-inertial mixed layer oscillations in the Bay of Bengal. *Oceanography*, **29** (2), 180–191.
- Johnston, T. M. S., and D. L. Rudnick, 2009: Observations of the transition layer. *Journal of physical oceanography*, **39** (3), 780–797.
- Johnston, T. M. S., D. L. Rudnick, N. Brizuela, and J. N. Moum, 2020: Advection by the North Equatorial Current of a cold wake due to multiple typhoons in the western Pacific: Measurements from a profiling float array. *Journal of Geophysical Research: Oceans*.
- Jullien, S., and Coauthors, 2012: Impact of tropical cyclones on the heat budget of the South Pacific Ocean. *Journal of physical oceanography*, **42** (11), 1882–1906.
- Kunze, E., 1985: Near-inertial wave propagation in geostrophic shear. *Journal of Physical Oceanography*, **15** (5), 544–565.
- Lien, R.-C., and T. B. Sanford, 2019: Small-scale potential vorticity in the upper-ocean thermocline. *Journal of Physical Oceanography*, **49** (7), 1845–1872.
- Mei, W., C.-C. Lien, I.-I. Lin, and S.-P. Xie, 2015a: Tropical cyclone-induced ocean response: A comparative study of the South China Sea and tropical northwest Pacific. *Journal of Climate*, **28** (15), 5952–5968.
- Mei, W., F. Primeau, J. C. McWilliams, and C. Pasquero, 2013: Sea surface height evidence for long-term warming effects of tropical cyclones on the ocean. *Proceedings of the National Academy of Sciences*, **110** (38), 15 207–15 210.
- Mei, W., S.-P. Xie, F. Primeau, J. C. McWilliams, and C. Pasquero, 2015b: Northwestern Pacific typhoon intensity controlled by changes in ocean temperatures. *Science advances*, **1** (4), e1500 014.
- Moum, J., D. Farmer, W. Smyth, L. Armi, and S. Vagle, 2003: Structure and generation of turbulence at interfaces strained by internal solitary waves propagating shoreward over the continental shelf. *Journal of Physical Oceanography*, **33** (10), 2093–2112.
- Niwa, Y., and T. Hibiya, 1997: Nonlinear processes of energy transfer from traveling hurricanes to the deep ocean internal wave field. *Journal of Geophysical Research: Oceans*, **102** (C6), 12 469–12 477.
- Pallàs-Sanz, E., J. Candela, J. Sheinbaum, J. Ochoa, and J. Jouanno, 2016: Trapping of the near-inertial wave wakes of two consecutive hurricanes in the Loop Current. *Journal of Geophysical Research: Oceans*, **121** (10), 7431–7454.
- Pinkel, R., 2014: Vortical and internal wave shear and strain. *Journal of physical oceanography*, **44** (8), 2070–2092.
- Pollard, R. T., and R. Millard Jr, 1970: Comparison between observed and simulated wind-generated inertial oscillations. *Deep Sea Research and Oceanographic Abstracts*, Elsevier, Vol. 17, 813–821.
- Powell, M. D., P. J. Vickery, and T. A. Reinhold, 2003: Reduced drag coefficient for high wind speeds in tropical cyclones. *Nature*, **422** (6929), 279–283.
- Price, J. F., 1981: Upper ocean response to a hurricane. *Journal of Physical Oceanography*, **11** (2), 153–175.
- Price, J. F., 1983: Internal wave wake of a moving storm. Part I. Scales, energy budget and observations. *Journal of Physical Oceanography*, **13** (6), 949–965.
- Price, J. F., T. B. Sanford, and G. Z. Forristall, 1994: Forced stage response to a moving hurricane. *Journal of Physical Oceanography*, **24** (2), 233–260.
- Sanford, T. B., J. F. Price, and J. B. Girton, 2011: Upper-ocean response to Hurricane Frances (2004) observed by profiling EM-APEX floats. *Journal of Physical Oceanography*, **41** (6), 1041–1056.
- Sanford, T. B., J. F. Price, J. B. Girton, and D. C. Webb, 2007: Highly resolved observations and simulations of the ocean response to a hurricane. *Geophysical Research Letters*, **34** (13).
- Shade, L. R., and K. A. Emanuel, 1999: The ocean's effect on the intensity of tropical cyclones: Results from a simple coupled atmosphere-ocean model. *Journal of the Atmospheric Sciences*, **56** (4), 642–651.
- Shay, L. K., R. L. Elsberry, and P. G. Black, 1989: Vertical structure of the ocean current response to a hurricane. *Journal of physical oceanography*, **19** (5), 649–669.
- Shay, L. K., A. J. Mariano, S. D. Jacob, and E. H. Ryan, 1998: Mean and near-inertial ocean current response to Hurricane Gilbert. *Journal of physical oceanography*, **28** (5), 858–889.
- Sriver, R. L., and M. Huber, 2007: Observational evidence for an ocean heat pump induced by tropical cyclones. *Nature*, **447** (7144), 577–580.
- Sun, H., and E. Kunze, 1999: Internal wave-wave interactions. Part I: The role of internal wave vertical divergence. *Journal of physical oceanography*, **29** (11), 2886–2904.
- Talley, L. D., 2011: *Descriptive physical oceanography: an introduction*. Academic press.
- Thompson, A. F., S. T. Gille, J. A. MacKinnon, and J. Sprintall, 2007: Spatial and temporal patterns of small-scale mixing in Drake Passage. *Journal of Physical Oceanography*, **37** (3), 572–592.
- Thompson, E. J., J. N. Moum, C. W. Fairall, and S. A. Rutledge, 2019: Wind limits on rain layers and diurnal warm layers. *Journal of Geophysical Research: Oceans*, **124** (2), 897–924.
- Thorpe, S. A., 1977: Turbulence and mixing in a Scottish loch. *Philosophical Transactions of the Royal Society of London. Series A, Mathematical and Physical Sciences*, **286** (1334), 125–181.
- Vincent, E. M., M. Lengaigne, G. Madec, J. Vialard, G. Samson, N. C. Jourdain, C. E. Menkes, and S. Jullien, 2012a: Processes setting the

characteristics of sea surface cooling induced by tropical cyclones. *Journal of Geophysical Research: Oceans*, **117** (C2).

Vincent, E. M., M. Lengaigne, J. Vialard, G. Madec, N. C. Jourdain, and S. Masson, 2012b: Assessing the oceanic control on the amplitude of sea surface cooling induced by tropical cyclones. *Journal of Geophysical Research: Oceans*, **117** (C5).

Voelker, G. S., P. G. Myers, M. Walter, and B. R. Sutherland, 2019: Generation of oceanic internal gravity waves by a cyclonic surface stress disturbance. *Dynamics of Atmospheres and Oceans*, **86**, 116–133.

Walsh, K., M. Fiorino, C. Landsea, and K. McInnes, 2007: Objectively determined resolution-dependent threshold criteria for the detection of tropical cyclones in climate models and reanalyses. *Journal of climate*, **20** (10), 2307–2314.

Wamsley, L., 2018: Dozens more feared dead in the philippines after typhoon triggers mudslide. *National Public Radio*, URL <https://www.npr.org/2018/09/17/648866035/dozens-more-feared-dead-in-the-philippines-after-typhoon-triggers-mudslide>.

Weissman, D., B. Stiles, S. Hristova-Veleva, D. Long, D. Smith, K. Hilburn, and W. Jones, 2012: Challenges to satellite sensors of ocean winds: Addressing precipitation effects. *Journal of Atmospheric and Oceanic Technology*, **29** (3), 356–374.

Yablonsky, R. M., and I. Ginis, 2009: Limitation of one-dimensional ocean models for coupled hurricane–ocean model forecasts. *Monthly Weather Review*, **137** (12), 4410–4419.

Zedler, S. E., 2009: Simulations of the ocean response to a hurricane: Nonlinear processes. *Journal of physical oceanography*, **39** (10), 2618–2634.